Combustion behavior of single iron particles-part I

Applications in Energy and Combustion Science 13 (2023) 100097

Contents lists available at ScienceDirect

Applications in Energy and Combustion Science

journal homepage: www.sciencedirect.com/journal/applications-in-energy-and-combustion-science

Combustion behavior of single iron particles-part I: An experimental study in a drop-tube furnace under high heating rates and high temperatures

Aidin Panahi [a,b,*], Di Chang [a], Martin Schiemann [c], Aki Fujinawa [d], Xiaocheng Mi [e], Jeffrey M. Bergthorson [d], Yiannis A. Levendis [a]

[a] Mechanical and Industrial Engineering Department, Northeastern University, Boston, MA, USA
[b] Department of Mechanical Engineering, Massachusetts Institute of Technology, Cambridge, MA, USA
[c] Department of Energy Plant Technology, Ruhr-University Bochum, Bochum, Germany
[d] Department of Mechanical Engineering, McGill University, Montreal, QC, Canada
[e] Department of Mechanical Engineering, Eindhoven University of Technology, Eindhoven, the Netherlands

ARTICLE INFO

Keywords:
Metal fuel
Iron
Combustion
Temperature
Burn-out time

ABSTRACT

Micrometric spherical particles of iron in two narrow size ranges of (38–45) μm and (45–53) μm were injected in a bench scale, transparent drop-tube furnace (DTF), electrically heated to 1400 K. Upon experiencing high heating rates (10^4–10^5 K/s) the iron particles ignited and burned. Their combustion behavior was monitored pyrometrically and cinematographically at three different oxygen mole fractions (21%, 50% and 100%) in nitrogen. The results revealed that iron particles ignited readily and exhibited a bright stage of combustion followed by a dimmer stage. There was evidence of formation of envelope micro-flames around iron particles (nanometric particle mantles) during the bright stage of combustion. As the burning iron particles fell by gravity in the DTF, contrails of these fine particles formed in their wakes. Peak temperatures of the envelope flames were in the range of 2500 K in air, climbing to 2800 K in either 50% or 100% O_2. Total luminous combustion durations of particles, in the aforesaid size ranges, were in the range of 40–65 ms. Combustion products were bimodal in size distribution, consisting of micrometric black magnetite particles (Fe_3O_4), of sizes similar to the iron particle precursors, and reddish nanometric iron oxide particles consisting mostly of hematite (Fe_2O_3).

1. Introduction

Renewable sources of energy are abundant on our planet. Harnessing solar, wind, hydro, and geothermal power can, in principle, eliminate the use of fossil fuels, thus, solving the energy and climate crisis faced by our society. Most of these renewable energy sources are, however, geographically scattered and highly intermittent. In order to reduce carbon emissions on a global scale, temporal and regional surplus of clean energy needs to be transformed into transportable, storable, and recyclable energy carriers [1]. Iron powders have been proposed as a promising circular fuel for long-term storage and long-distance transport of clean energy owing to their carbon-free nature, high energy density, and recyclability after combustion [2–6]. To make the iron-fuel-based cycle of renewable energy a reality, a bottleneck is to develop practical combustors that can efficiently release the chemical energy carried by iron powders in a controllable fashion. To this end, a better understanding of the fundamentals underlying the combustion of fine (micrometric) iron particles is required.

An advantage of iron powders as a circular fuel, as mentioned above, is the potential of very high recyclability after combustion. What gives rise to this advantage is the high melting and boiling points of iron and iron oxides (FeO, Fe_3O_4, and Fe_2O_3). A micrometric iron particle remains mostly in condensed (i.e., solid and liquid) phases throughout its combustion process in air and environments with even greater oxygen concentrations. Therefore, two unique features rooted in iron-particle combustion cannot be adequately explained with our existing knowledge in combustion of gaseous and volatile solid fuels: (I) Propagation dynamics of a spatially discrete flame, and (II) heterogeneous oxidation mechanisms of a micrometric iron particle.

Since the oxidation process of a burning iron particle takes place at its surface, the released heat is first highly concentrated in the immediate vicinity of the particle, then, diffuses away from the particle, and ignites its unburnt neighbors. A flame thus propagates in a suspension of iron particles. This flame propagation dynamics can be characterized by

* Corresponding author at: Mechanical and Industrial Engineering, Northeastern University, Boston, MA, USA.
E-mail address: panahi.a@northeastern.edu (A. Panahi).

https://doi.org/10.1016/j.jaecs.2022.100097
Received 13 July 2022; Received in revised form 29 October 2022; Accepted 5 November 2022
Available online 6 November 2022

two key time scales [7]: (1) The burning time of each particle, t_r, i.e., over which it releases energy; (2) the characteristic time of heat diffusion from one particle to its neighbors, t_d. If $t_r \gg t_d$, i.e., the energy release from each particle is much slower than the heat diffusion to its neighbors, the flame structure (in terms of gas temperature and oxygen concentration) is spatially continuous, resulting in a propagation behavior similar to that of gaseous flames. If $t_r \ll t_d$, i.e., the energy release of each particle is much faster than inter-particle heat diffusion, the flame, with a spatially discrete structure, propagates via a mechanism fundamentally differing from that of continuous flames. In suspensions of discrete reactive particles, radiative heat transfer (which can be effective over much larger length scales [8]) is important and it may also contribute to preheating of the unburnt dust. A comprehensive review on the experimental and theoretical efforts made towards understanding *discrete flames* can be found in Ref. [9].

A series of experimental studies—ranging from flames stabilized in Bunsen [10] and counterflow [11] burners to flames propagating in a tube filled of dispersed iron particles at various levels of gravity [12–16]—has been carried out by researchers at McGill University over the past decade, gaining insights into the unique Feature (I) of iron combustion. Under certain conditions created in these experiments, e.g., in a gaseous medium with a low thermal diffusivity, a weak dependence of flame speed on oxygen concentration can be identified as a possible evidence of discrete flame propagation [11,14,15]. A reduced-order model based on the reaction-diffusion equations—the discrete-source model—with prescribed conditions of $t_r \ll t_d$ captures flame morphologies qualitatively resembling those of experimentally identified discrete flames [7,17]. With an *ad-hoc* input of experimentally measured t_r, the discrete-source model can determine whether the flame is under a continuous or discrete regime of propagation in a good agreement with the corresponding experimental observation [13]. The question thus arises as to whether t_r—the burn time of an iron particle—can be estimated *a priori* or solved dynamically within a flame-propagation model. To answer this question, a more in-depth understanding is required into the complex heterogenous oxidation processes of iron particles, previously stated as the unique Feature (II) of iron-particle combustion. A new thread of research investigating the combustion process of isolated iron particles in different oxidizing environments was thus initiated.

The first study of this new thread of research was carried out by Wright et al. [18]. These authors measured both the time to maximum light intensity (t_{max}) and the burnout time (t_{tot}) of iron particles, over a size range from 25 to 75 μm, injected into, and ignited by, a hot flow of argon-oxygen mixtures with various oxygen concentrations. For pure iron particles, both of these burn times as a function of particle size can be fitted by a power law with exponents significantly less than 2, i.e., 1.32–1.67 for t_{max} and 1.25–1.67 for t_{tot}. As a d^2-law of particle burn time indicates that the oxidation rate of a burning particle is controlled by the external diffusion of oxidizer (i.e., from bulk gas to particle surface) [19], the identified low power-law exponents suggest that the burnout of iron particles is influenced by the condensed-phase kinetics and by more complex oxygen transport processes across the gaseous boundary layer, e.g., Stefan flow. A recent study by Ning et al. [20], reported burn times of laser-ignited iron particles, over a size range of 25–54 μm in oxygen-nitrogen gaseous mixtures with various oxygen mole fraction between 21% and 36%; further confirming a particle-size dependence significantly weaker than a d^2-law for both t_{max} and t_{tot}. Those authors also found that t_{max} is nearly reversely proportional to the concentration of oxygen over a range in X_{O_2} between 26% and 36%. This finding suggests that the combustion process of an iron particle is first limited by the rate of external oxygen diffusion and then partially controlled by the kinetics inside the particle. To gain further insights into this interplay between external diffusion of oxidizer and liquid-phase iron oxidation kinetics, *in-situ* measurement of the light intensity and temperature of burning iron particles were then attempted by the researchers.

The time-resolved measurements of light intensity of isolated burning iron particles ignited by a laser [20] and hot gas flow produced by $CH_4/O_2/N_2$ flames [5] demonstrate some features in common: (a) A brief plateau shortly after the ignition (i.e., when particle light intensity first becomes detectable) likely corresponding to the process of melting. (b) A monotonic increase to a maximum intensity followed by a decrease while the particle likely remaining in liquid phase. (c) An abrupt, small increase occurs when the intensity decreases to nearly the same level of the melting plateau (Feature 1), followed by the light of the particle fading away. This jump is hypothetically attributed by Ning et al. [20] to a rapid release of latent heat upon the crystallization/solidification of a supercooled Fe/O droplet.

In a later publication of Ning et al. [21], time-resolved temperature measurement of burning iron particles is reported for the first time in literature, supporting the phase-change interpretation of the features identified in the time history of light intensity. Alas, the data of time-resolved temperature of burning iron particles are still very limited in the literature. Ning et al. [21] reported the result for only one case—particles with a mean diameter of 54.34 μm burning in air, and the data provided by Li et al. [5] is likely influenced by more complex oxidative reactions between iron and the products of a methane-oxygen flame. More extensive studies of isolated-iron-particle combustion with time-resolved temperature measurements are needed.

A further complication of iron-particle combustion is that a relatively small amount of liquid Fe-O mixture evaporates, reacts with oxygen in gas phase, and re-condenses to Fe_2O_3 nanoparticles. This conjecture is supported by multiple experimental evidence. FeO molecular lines can be detected in the gaseous emission spectrum of isolated burning iron particles and flames [10,11,14]. A significant size increase of a burning iron particle until reaching the maximum light intensity, generating a plume- or halo-like cloud surrounding the particle, were observed [14,22–24]. This surrounding cloud is interpreted as the locus where the gaseous oxide products condense to nanoparticles. Using high-speed and high-magnification shadowgraph, Ning et al. [23] recorded the time evolution of the nanoparticle cloud synchronized with the measurement of particle temperature. The results show that the formation of nanoparticle terminates slightly after the particle reaching its peak temperature. Based on the thermo-equilibrium calculation, indicating that the vapor pressure of liquid iron is an order-of-magnitude greater than those of liquid FeO and Fe_3O_4, Ning et al. [23] hypothesized that the formation of nanoparticles is initiated due to the evaporation of liquid iron and ceases after liquid iron is burnt out. Scanning electron microscopy (SEM) images of combusted oxide particles show nanoparticles deposited on the surface of micrometric particles [5,11,14,20–22,25,26]. The condensation cloud and deposition of iron-oxide nanoparticles are more evident for iron particles burning in a gaseous mixture with greater oxygen concentrations [14]. Some insights gained into flame synthesis of iron-oxide nanoparticles [27] are useful to understand the vapor-phase iron oxidation and condensation processes underlying nanoparticle formation in the combustion of micron-sized iron particles.

The current study aims to extend the set of experimental data monitoring the combustion process of iron particles under various oxidizing conditions (in Part I), and thus, to deepen the theoretical interpretation of the observed combustion characteristics and the underlying mechanisms (in Part II) [28]. This paper (Part I) reports on combustion of single iron particles in the constant gas temperature environment of an electrically heated drop-tube furnace (entrained reactor) [29–33]. Particle combustion occurred at a gas temperature of 1350 K and a furnace wall temperature of 1400 K. The heating rate which the injected iron particles experienced was high, being in the order of 10^4 K/s [34,35]. Three ambient gas compositions were implemented: 21% O_2 – 79% N_2 (i.e., air), 50% O_2 – 50% N_2 and 100% O_2 (neat oxygen). Two different micrometric iron particle sizes were burned, in rather narrow particle size cuts: 38–45 μm and 45–53 μm. Combustion histories of single particles were assessed by both three-wavelength optical pyrometry and high-speed cinematography to

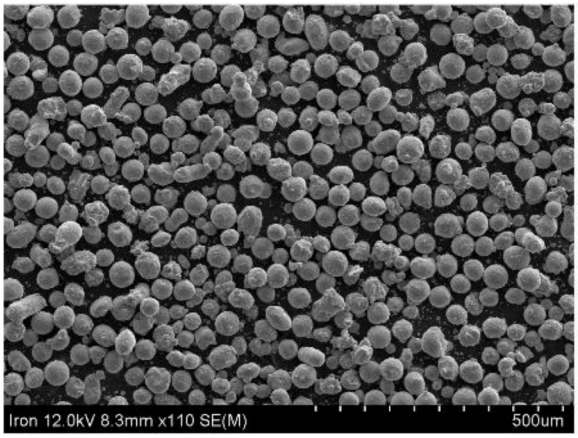

Fig. 1. Scanning electron microscopy images of iron particles (38–45 μm).

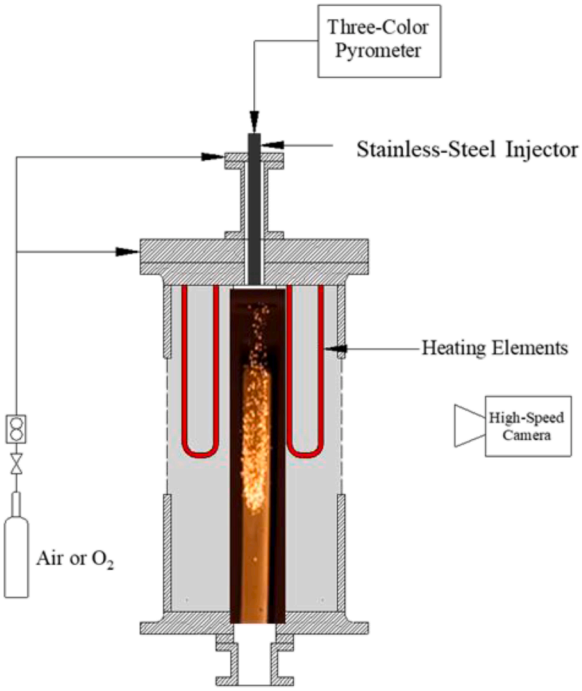

Fig. 2. Schematic illustration of the drop tube furnace, iron particle introduction and combustion therein. This image depicts combustion of a stream of (53–75) μm iron particles burning in air.

obtain their burnout times and time-resolved particle temperatures. The roles of oxygen concentration in the gas and of the particle size on these combustion parameters were investigated. Pyrometric and cinematographic observations on their combustion behaviors were recorded. Condensed-phase products of iron particle combustion were captured and examined.

2. Materials and experimental methods

2.1. Iron particles

Iron particles were supplied by *TLS Technik GmbH & Co* in Germany. All iron fuels were size-classified by sieving to obtain size cuts of (38–45) μm and (45–53) μm. The particle morphology and dimensions are shown in the photograph displayed in Fig. 1, taken by SEM.

2.2. Experimental apparatus

Combustion of the iron particles was conducted in an electrically heated laminar-flow drop-tube furnace manufactured by *Applied Test Systems* (ATS). The furnace was fitted with a transparent quartz tube with an inner diameter of 7 cm. The length of the radiation zone is 25 cm, and it is heated by eight hanging $MoSi_2$ elements. The iron particles were introduced through a water-cooled stainless-steel injector, 61 cm long and 1.25 cm inner diameter, and the oxidizing gas was introduced through a flow straightener, positioned coaxially to the particle injector. The oxidizing gas was either air or O_2/N_2 gas mixtures containing 50% or 100% O_2 by volume. The flowrate of gas was set at 0.5 l/min. In these single particle experiments no gasses were introduced through the furnace injector. A very small quantity of fuel particles were scooped by the tip of a beveled needle syringe and were released into the furnace injector by a gentle tap. The furnace wall temperature was maintained at 1400 K and the gas temperature at the furnace centerline was measured with radiation-corrected thermocouples to be ~1350 K for most of the length of the 25 cm long radiation zone [31,34]. The heating rate of the particles was determined from the profile of the measured gas temperature along the axis of the drop tube furnace (DTF), T_{gas}, starting at the exit of the water-cooled particle injector. For this purpose, fine, type K thermocouples were used, subjected to appropriate radiation corrections, see Refs. [31,36]. This particle heating rate was also confirmed by backlight cinematographic recordings of the initial entrance of a (backlit) particle from the tip of the injector into the furnace and the first appearance of luminous combustion (ignition by the onset of a luminous flame).

The experimental combustion setup is depicted in Fig. 2, where the combustion of a stream of iron particles is also exemplified. When particles were injected in this furnace, they ignited and burned with a temperature jump. In single particle experiments, their temperatures were measured pyrometrically from the top of the furnace, along the free-fall trajectory of each particle. Thus, the luminous burnout histories of single iron particles from ignition to extinction could be monitored. The travel distances of iron particles, under the conditions of this study, were in the order of centimeters, including both their ignition delay period and their burnout period. In addition to pyrometry, high-speed high-resolution cinematography was conducted from the side of the furnace, see Fig. 2, using an *Edgertronic* camera, fitted with a long-range microscope *Infinity* lens. A particular advantage of the configuration experimentally investigated here is that the far-field boundary conditions (i.e., gas composition and gas temperature) are well defined over the entire course of a particle's trajectory.

2.3. Three-Color pyrometer and calibration

Light from burning iron particles was focused by an inverted collimating lens on one end of an optical fiber (*General Fiber Optics*), and it was transmitted to the optical pyrometer of Levendis, Estrada, and Hottel [37]. This pyrometer employs two dichroic edge filters as spectrum splitters to direct the light to three photodetectors. Radiation is thus carried to the first spectrum splitter (*Newport*) mounted at 45° on a rotating stage (*Melles Griot*). At this angle, the splitter has a reflecting wavelength window spanning from 0.60 to 0.70 μm. A second dichroic splitter (*Newport, 10QM20HL.11*), with a reflecting window from 0.74 to 0.82 μm, is placed further along the light path, at an angle of 26.6°, to split the remaining portion of the spectrum between the two remaining channels. Three medium band-width interference filters (*Oriel*) with full width at half maximum (FWHM) of 70 nm are used to define the working wavelengths of 0.640, 0.810 and 0.998 μm. Hence, the absorption bands of water vapor and carbon dioxide are avoided and there is only minimal interference from the elemental lines of sodium and potassium (589 nm and 766 nm, respectively).

The monochromatic emissive power (spectral radiation intensity) of a blackbody at temperature, T, is given by Planck's law [37]:

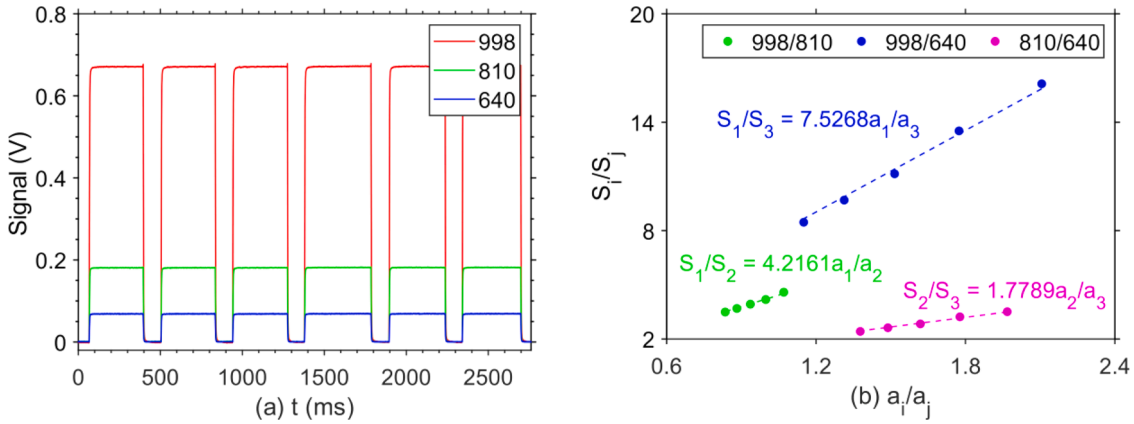

Fig. 3. (a) Calibration lamp signals captured by pyrometer, (b) the slopes of linear fits are the calibration coefficients.

$$I_{\lambda b} = \frac{c_1}{\lambda^5\left(e^{\frac{c_2}{\lambda T}} - 1\right)} \tag{1}$$

Since burning iron particles are not necessarily blackbodies, their spectral emissivity,$\varepsilon_{\lambda,T}$, needs to be accounted for. Then the monochromatic emissive power for the particles becomes:

$$I_{\lambda} = \frac{\varepsilon_{\lambda,T} c_1}{\lambda^5\left(e^{\frac{c_2}{\lambda T}} - 1\right)} \tag{2}$$

The spectral emissivity of a surface,$\varepsilon_{\lambda,T}$, is a function of both the wavelength of emission and the temperature of the particle. The monochromatic emissive power of a non-blackbody surface of area A is:

$$E_{\lambda} = \varepsilon_{\lambda} I_{\lambda b} A \tag{3}$$

The total emissive power of a non-blackbody surface with area A is given by integrating E_{λ} over the entire spectrum would be:

$$E(T) = \int_0^{\infty} \varepsilon_{\lambda} I_{\lambda b} A d\lambda \tag{4}$$

Two methods (the pyrometric signal ratio method and the nonlinear least square method) were employed and used to calculate particle temperature in this paper, based on the generated three-color voltage signals of the optical pyrometer, the wavelength dependences of the transmittances of the dichroic and the interference filters, as well as the responsivities of the detectors, as described in Ref. [38]. This caused considerable mathematical complexity but enhanced the calculation accuracy.

(a) The pyrometric signal ratio method was used to calculate three temperatures based on particle radiation intensity signals obtained at the three wavelength ratios (S_{999}/S_{810}, S_{810}/S_{640}, S_{999}/S_{640}) and accounting for the efficiencies of all the pyrometer components, thus improving on the simplified ratio pyrometry method of Levendis et al. [37] . For this three-wavelength instrument, Eq. (5) is used to derive the signal ratios, upon cancelation of the luminous area term, A, at each instant of time, as shown in Eq. (5).

$$\frac{S_i}{S_j} = \frac{C_i \int_{\Delta\lambda_i} \varepsilon_{\lambda_i} I_{\lambda b} g_i(\lambda) d\lambda}{C_j \int_{\Delta\lambda_j} \varepsilon_{\lambda_j} I_{\lambda b} g_j(\lambda) d\lambda} = C_i a_i \Big/ C_j a \tag{5}$$

where $C_i$and C_j are calibration constants, $S_i$and S_j are measured voltage signals by the pyrometer at different channels. Substitution of Eq. (2) in Eq. (5) can lead to solution for temperature, if the emissivity is known. Further details and the solution for temperature are given in Ref. [37].

Since the emissivity of the burning iron particles is not independently known, the assumption that the particle emissivity does not change with wavelength in the range of 640 to 998 nm was made, i.e., the gray body radiation assumption.

(b) The non-linear least-square method was used to determine the most probable distribution of Planck's law that minimizes the sum of squared errors $\sum \Delta^2$ between measured signals (S shown in Eq. (5)) and calculated signals (s), as indicated below in Eqs. (6) and (7).

$$\sum_{n=1}^{3} \Delta_n^2 = \sum_{n=1}^{3} (S_n - s_n)^2 \tag{6}$$

$\sum_{n=1}^{3} \Delta_n^2$ is a function of both temperature and area,$\sum_{n=1}^{3} \Delta_n^2 = f(T, A)$, and the calculated voltage signal in channel n is obtained from Eq. (7):

$$s_n = E(T) = A \int_{\Delta\lambda_n} \varepsilon_{\lambda} I_{\lambda b} g_n(\lambda) d\lambda \tag{7}$$

where n can be 1, 2 or 3 representing the 998, 810 and 640 nm pyrometer channels, respectively, and $g_n(\lambda)$ is the wavelength function of the combined transmittance of the associated dichroic filter (τ_d), the associated interference filter (τ_i) and the associated responsivity of photo-detectors (R_{pd}) for channel n. The first order partial derivatives of the function with respect to all independent variables, i.e. T, A, are then taken and set equal to zero at the extremum points. These are two equations with two unknowns T, A. To obtain a solution for T, each of the above equations is first solved for A. Then A is eliminated between the two ensuing equations by setting them equal to each other and, subsequently, a solution for T is obtained iteratively. Further details of this method are given in Ref. [37].

Calibration of the pyrometer was conducted using a tungsten lamp. A pre-calibrated gas-filled tungsten filament lamp, model S6–100, was obtained from *Pyrometer LLC* (New Jersey, USA). Apparent temperature values were provided by the vendor at 0.65 μm, against lamp current. The true temperatures of the lamp were calculated from five apparent temperatures, T_a, of 2073 K, 2173 K, 2273 K, 2373 K, and 2473 K using emissivity values for tungsten provided in Ref. [39]. During calibration of the pyrometer, the tungsten lamp was placed at the bottom of the furnace, and its radiation intensity signals were recorded, viewing from the top of the furnace, in an environment where the lamp was the only light source. The lamp-generated signals were chopped, as exemplified in Fig. 3a. According to Eq. (5), the integral ratios of a_i/a_j were calculated, and the signal ratios S_i/S_j were obtained from the pyrometer, as

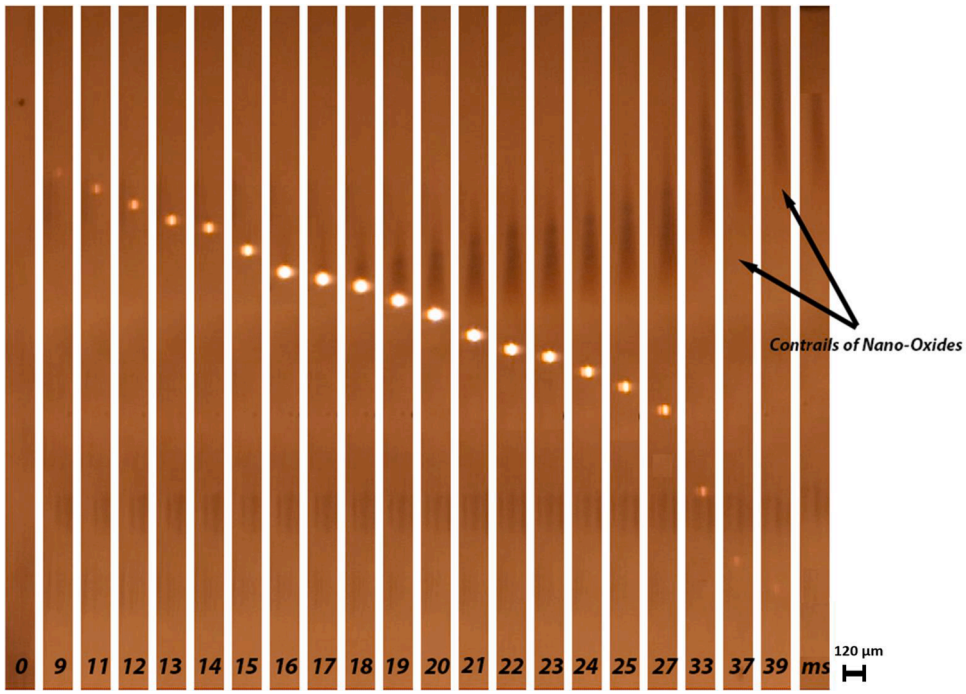

Fig. 4. A photographic time sequence from backlight cinematography of one ~40 μm single iron particle burning in air.

Fig. 5. Photographic sequence from backlight cinematography using a neutral density filter of one ~40 μm single iron particle burning in air. The photographic stills are 1 ms apart and the center image (number 4) was at the peak of the detected particle brightness.

explained in [37]. Then the calibration coefficients C_i/C_j were derived to be C_1/C_2=4.2161, C_2/C_3=1.7789, and C_1/C_3=7.5268, respectively, as shown in Fig. 3b. Subsequently, a code was written in *MATLAB* software using these coefficients to calculate the true particle temperature.

3. Results and discussion

3.1. Cinematographic observations on burning single iron particles

Combustion of single iron particles was observed with high-speed, high-resolution cinematography, as exemplified in Fig. 4 with a sequence of frame stills. The photographic history of a single iron particle, from the 38–45 μm size cut, is shown burning in air. Upon exiting the furnace injector and entering the radiation cavity of the furnace, the particle (shown as a black dot in the first frame of Fig. 4) heated up and ignited (shown as the ensuing orange images in Fig. 4). Upon ignition, the luminosity of the burning particle increased. The particle size also appears to have increased. Eventually the luminosity subsided, and the particle size appeared to shrink again. The size of the particle before and after ignition was compared with the size of a metallic platinum wire of 120 μm in diameter, which was inserted in the furnace to provide size calibration. Given that the initial particle size was of approx. 40 μm, the maximum observed size of the iron particles appeared to be also 120 μm. However, it became apparent that the bright images of the particle were enlarged by overexposure of the image intensity (i.e., as the maximum intensity level, 255, of the 8-bit digital image was exceeded in a number of frames), due to the very bright light emitted by the burning iron particles. To avoid overexposure of the images, a neutral density filter was mounted on the camera lens. A number of snapshots of another iron particle burning in air through an optical filter with a 0.2 density are shown in Fig. 5. These snapshots correspond to the high brightness segment of the particle burnout history. They were used to determine the actual size of the flame. Based on these photographs, the flame size of this burning particle appears to be ~ 60 μm. Still, this is significantly larger than the size of the ~40 μm iron particle injected in the furnace.

At this point it should be clarified that most likely, based on earlier reports [22,40] and modeling efforts in the present investigation [28] the particle is in the form of a liquid droplet. According to the literature, it is either liquid iron or liquid iron oxide or a mixture of both [20,21,41]. This is also supported by the findings of Li et al. [22], Huang et al. [40] and Palecka et al. [14], as when the melting point of iron is reached ($T_{melting(Fe)}$ = 1811 K), the particle melts and becomes fully liquefied. According to Glassman's simplified paradigm [42], if the flame temperature is below the metal fuel's boiling point ($T_{boiling(Fe)}$ = 3133 K), the combustion should proceed with heterogeneous surface oxidation. For iron particles, since the majority of combusted products remain as micrometric particles, the combustion is indeed mostly heterogeneous; as the combustion generally happens above the melting points of iron and its oxide, there must also be a certain amount of evaporation, even at temperatures below the boiling point. However, this evaporation rate is too slow to consume the inward transported oxygen at the corresponding stoichiometric ratio. Thus, this makes it unlikely that a lifted micro-flame envelope would form, like that observed for a burning aluminum particle [42].

On the other hand, the evaporated Fe is oxidized to FeO and FeO_2 in vapor phase, likely with a gaseous reaction layer very closely attached to

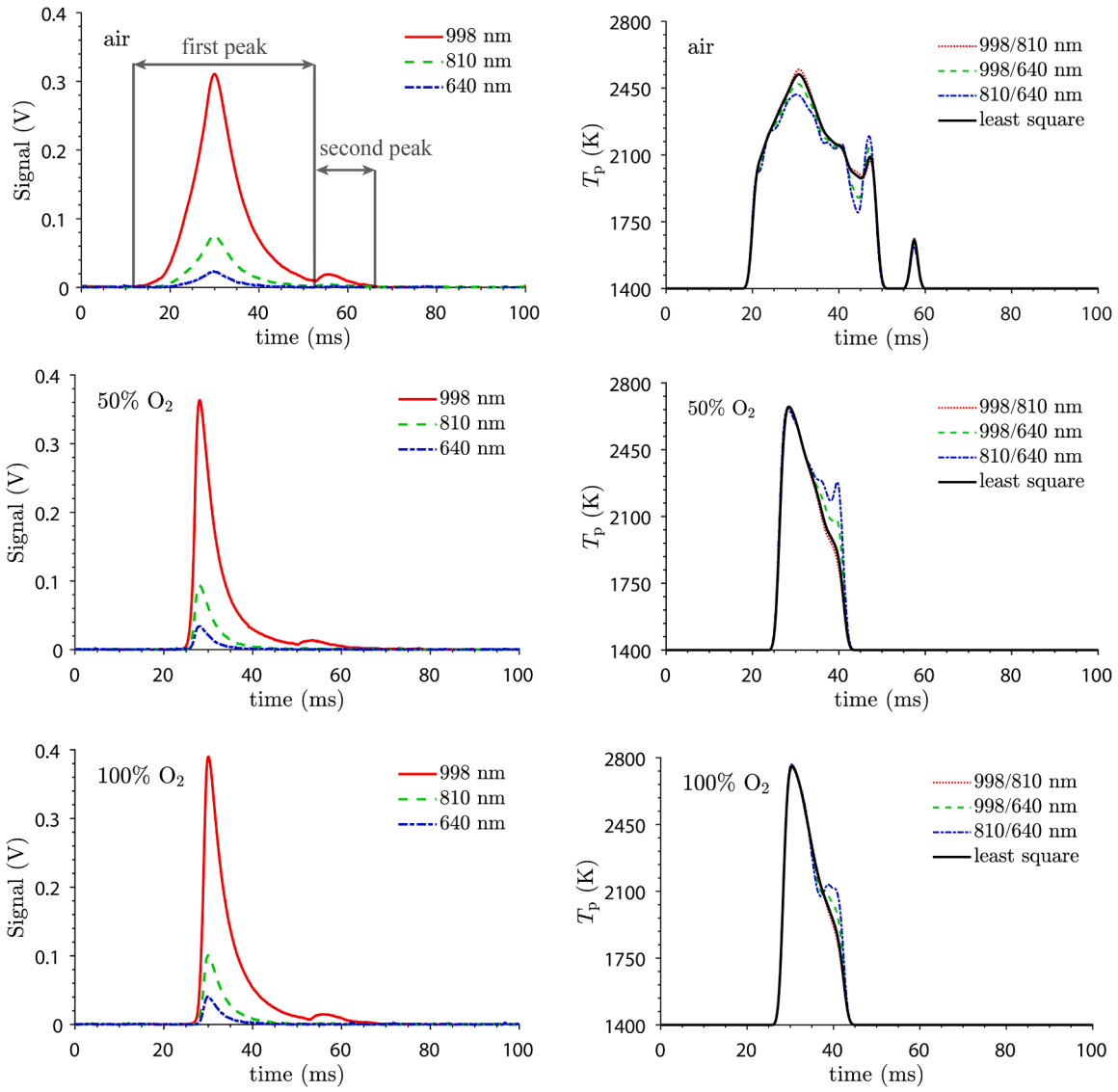

Fig. 6. Deduced temperature-time profiles obtained from pyrometry of single particles of 38–45 μm iron burning in air (top row), 50% O_2 (middle row), and 100% O_2(bottom row). All temperature profiles (right column) were subjected to data smoothing to minimize the presence of noise, which is caused by weak radiation at the tail end of each signal (left column).

the particle surface. As these gaseous iron oxides diffuse away from the particle, with a decrease in temperature, they condense to Fe_2O_3 nanoparticles, likely following a pathway as that hypothesized (and partly identified) for combustion synthesis of iron-oxide nanoparticles [27]. The ongoing reaction between iron and dissolved oxidizing gas on the liquid iron surface then further increases the particle temperature until reaching its maximum where particle micro-explosions may occur, as has been reported in [22,40] and also observed herein. Evidence for vapor-phase combustion and FeO formation was also observed in prior microgravity experiments and ground tests [10]. As the evolving metal or metal suboxide vapors sequentially cool and supersaturate, causing fine droplets to nucleate and subsequently grow to form ultra-fine (nanometric) particles, they generate an aerosol in the vicinity of the particle [27]. This is evident by the buoyant dark plume photographed during the middle and final stages of the burning iron particle shown in Fig. 4. These nanometric particles aggregate and form contrails behind the free-falling particles in the drop tube furnace. Eventually, they are forced to settle, carried by the gas flow, to the bottom of the drop-tube (entrained flow) furnace. Therein, they are collected on a paper filter, along with solidified micrometric iron oxide particles.

3.2. *Pyrometric observations of particles burning at different oxygen partial pressures*

The three-color radiative intensity-time signals, generated by the pyrometer, for each burning iron particle were used to obtain temperature profiles. Fig. 6 displays the three time-resolved signals (S_{640}, S_{810}, S_{998}) of two different iron particles burning in air, in 50% O_2 and in 100% O_2. The signals increased to a maximum and then decreased, reflecting major contributions from the evolution of particle temperatures and minor contributions from the increase in radiating size of the flame. Pyrometric particle temperatures, also shown in Fig. 6 below the corresponding intensity signals, were calculated by both the pyrometric signal ratio method and the non-linear least-square method. All particles exhibited a spontaneous temperature rise, caused by exothermic oxidation reactions. Particle temperatures increased with increasing oxygen mole fractions in the gas, as illustrated by comparing the recorded values at the 21% O_2 and 50% O_2 cases. However, at higher oxygen mole fractions the temperatures did not appear to increase any further, since the recorded values at 50% O_2 were similar to those at 100% O_2. Upon ignition of the particles, in each case, their measured

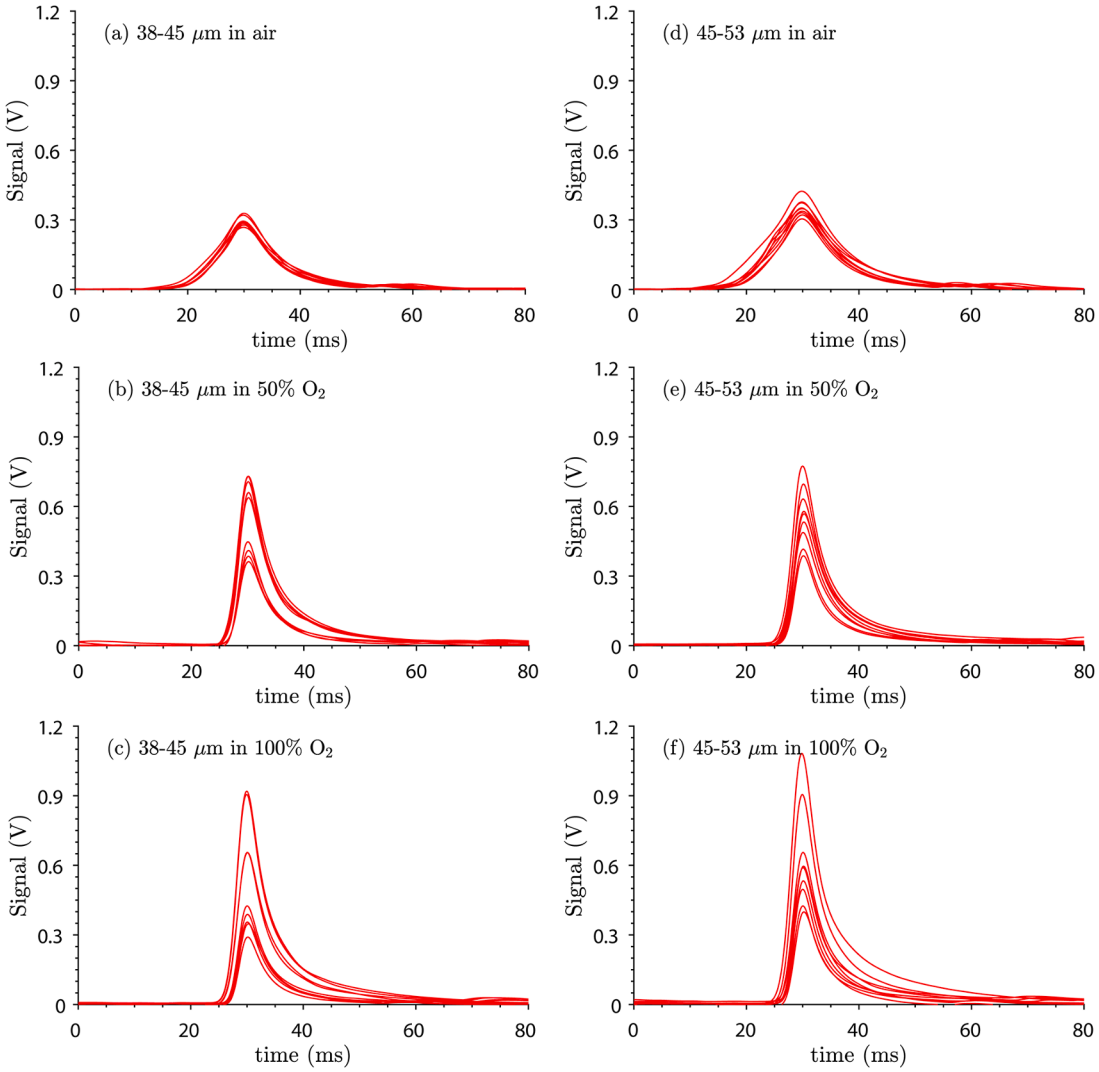

Fig. 7. Superimposed radiation intensity profiles ($S_{\lambda=998\ nm}$) of 10–12 iron particles burning in different ambient oxygen partial pressures in nitrogen, (a) particle size of 38–45 μm in air, (b) particle size of 38–45 μm in 50%O_2, (c) particle size of 38–45 μm in 100%O_2, (d) particle size of 45–53 μm in air, (e) particle size of 45–53 μm in 50%O_2, and (f) particle size of 45–53 μm in 100%O_2.

temperatures expediently increased above the melting point of iron (1811 K) and peak temperatures exceeded 2450 K in the case of air, whereas in the cases of 50% and 100% O_2 they exceeded 2750 K. These temperatures were calculated with the gray body assumption, i.e., with the emissivity assumed constant in the wavelength range of 640–998 nm. This assumption appears to be valid, since the three-color temperatures ($T_{998/810}$, $T_{810/640}$, $T_{998/640}$) were nearly identical for most of the particle profile durations, with the exception of the late-stage burnout sector of the profiles. This assumption of constant emissivity in the aforementioned wavelength range is also supported by the works of Krishnan et al. [43] and Muller et al. [41]. It is not clear whether the envelope micro-flame (nano-particle mantle) or the burning surface of the parent micrometric particle contributes most to the visible radiation emanating from the burning particles. Regarding the radiation from the nano-particle mantle, it is worth noting that gray body radiation was previously shown to be a valid assumption for approximating maximum temperatures of non-isothermal fine particle (soot)-laden envelope flames [33] engulfing similar-sized polymer (plastic) particles. Prior relevant publications also assumed that burning iron particles are gray body radiators [21,22], and this result appears to validate their assumption. The assumption of gray body radiation is not certain at the tail end of the particle burnout time after the extinction of the nano-particle mantle. In that profile sector the radiation of the remaining particle was weak and the noise to signal ratio was high. This may be partly attributed to the presence of the nano-particle contrail, see Fig. 4, which is likely to have interfered with the line of sight of the pyrometer.

The radiation profiles of particles typically exhibit two peaks, as depicted in Fig. 6. The second peak is much smaller than the first peak, and its presence has also been reported in previous publications [5,21,44]. Millot et al. and Ning et al. [21,44] postulated that the second peak is due to the rapid solidification of the supercooled molten O/Fe droplet, resulting from the fast latent heat release heating up the iron particle. Maximum temperatures in the second peak correspond to approx. 1800 K, in the vicinity of the melting point of magnetite.

3.3. *Pyrometric observations of particles of two different sizes burning at different oxygen partial pressures*

Iron particles of two different size cuts, (38–45) μm and (45–53) μm, were burned at different oxygen partial pressures (21%, 50% and 100%) in nitrogen. A number (more than 10 particles in each case) of superimposed radiation signal profiles, recorded by the 998 nm wavelength channel ($S_{\lambda=998}$) of the pyrometer are shown in Fig. 7. This channel, among the three channels of the pyrometer, generates the strongest signal. Signals typically experience two peaks, as mentioned before, however, the second peak is more pronounced in air than in the higher

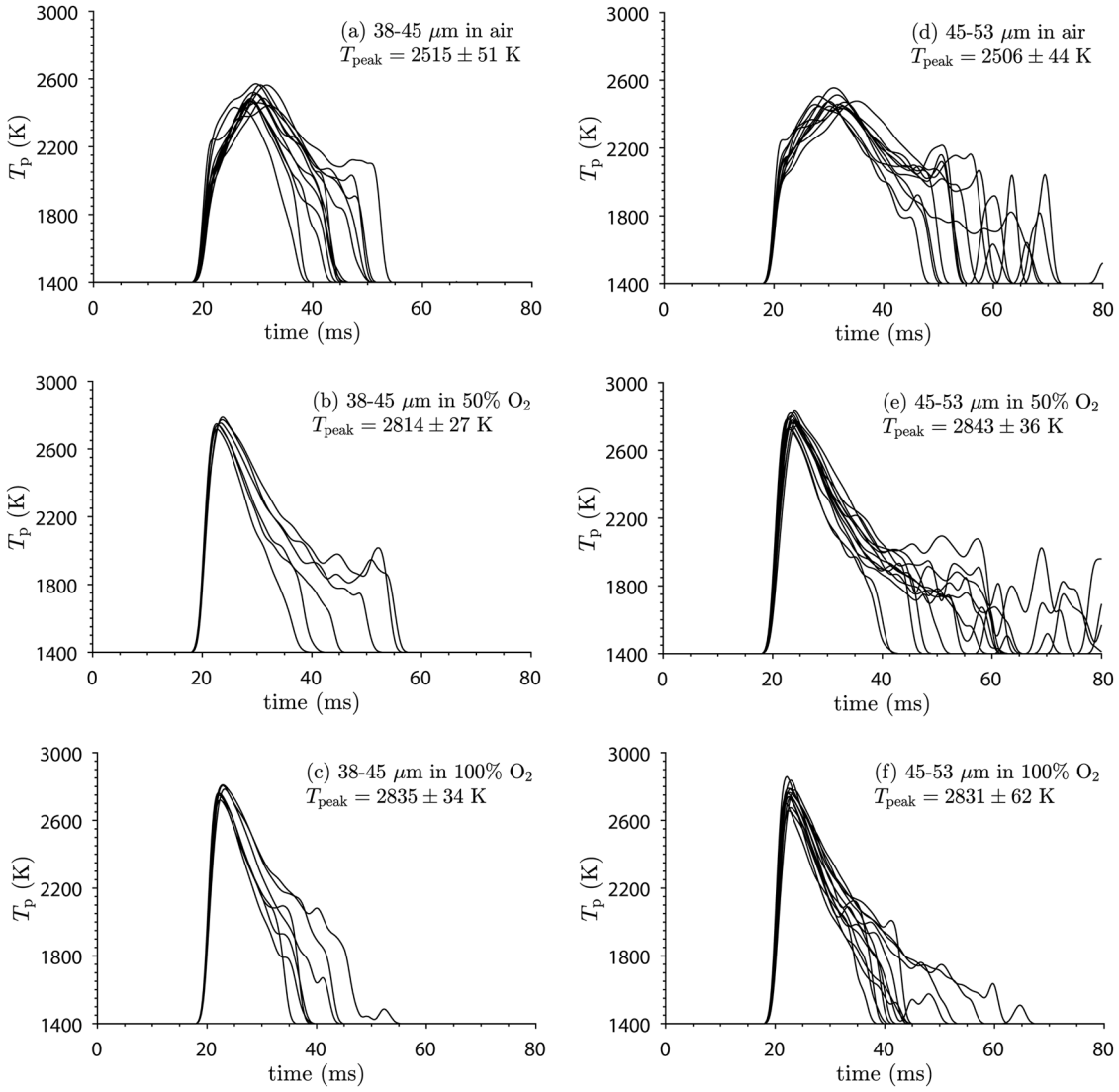

Fig. 8. Superimposed temperature-time profiles of 10–12 iron particles burning in different ambient oxygen partial pressures in nitrogen, (a) particle size of 38–45 μm in air, (b) particle size of 38–45 μm in 50%O_2, (c) particle size of 38–45 μm in 100%O_2, (d) particle size of 45–53 μm in air, (e) particle size of 45–53 μm in 50%O_2, and (f) particle size of 45–53 μm in 100%O_2.

Table 1
Luminous combustion times, based on pyrometric intensity signals ($S_{\lambda=998}$).

Surrounding Gas	Duration of the first peak (ms)		Duration of the second peak (ms)		Total combustion duration	
	38–45 μm	45–53 μm	38–45 μm	45–53 μm	38–45 μm	45–53 μm
Air	41.4 ± 2.8	45.3 ± 4.4	13.3 ± 1.1	14.2 ± 1.2	54.7 ± 3.6	59.5 ± 5.3
50%O_2–50% N_2	40.3 ± 7.2	43.3 ± 6.6	12.7 ± 1.2	14.1 ± 1.9	53.0 ± 8.1	57.4 ± 8.1
100%O_2	38.9 ± 11.8	39.1 ± 10.1	12.5 ± 2.6	13.6 ± 1.6	51.4 ± 11.8	52.7 ± 10.1

oxygen mole fractions containing gas. Corresponding temperature-time profiles of burning iron particles, recorded with three-color pyrometry and calculated with the non-linear least square method are shown in Fig. 8. The mean maximum temperatures of the first peak of the single particle of iron burning in air, 50%O_2 and 100%O_2 for two size cuts of (38–45) μm and (45–53) μm are depicted in Fig. 8, whereas the combustion durations of the particles are listed in Table 1. For the particle size of 38–45 μm, the mean maximum temperature of the iron particles burning in air is around 2515 K; it increases to 2814 K with the increase of oxygen concentration to 50%. However, the mean peak temperature further increases by only 21 K to 2835 K when the oxygen concentration increases to 100%. Such a temperature difference is not significant, as it is within the particle-to-particle variation error band. Hence, it can be concluded that oxygen mole fractions above 50% do not appear to affect the peak particle temperature. This observation was also made by Ning et al. [21], who reported that such a temperature plateau with increasing oxygen mole fraction in the surrounding gas commenced even at lower oxygen mole fractions. This plateau is likely due to the balance between the increases in both heat release rate and evaporative heat loss rate at greater O_2 concentrations. Regarding the effect of the particle size on temperature, it appears that particles of both 38–45 μm and 45–53 μm diameters experience similar maximum temperatures, see Fig. 8. Hence, for all particles in the examined 38–53 μm range, the effect of particle size on the maximum temperature appears to be negligible, under the conditions of these experiments where ambient temperatures were high. The negligible change in peak temperature with particle size is likely due to the fact that the increase in the thermal capacity of a particle, scaling with d^3, compensates and slightly overweighs the increase in heat release rate, roughly scaling with d^2.

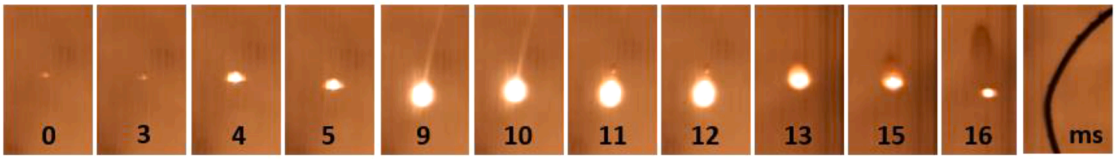

Fig. 9. An illustration of an iron particle undergoing bursting micro-jects of molten matter from particles in neat oxygen. The last frame of this photograph shows the image of a section of a metallic platinum wire of 120 μm in diameter, which was inserted in the furnace to provide calibration for the initial particle size.

Previous work by Ning et al. [21] reported significant temperature difference in a similar particle-size range, with larger particles reaching more elevated peak temperatures. Further discussion of this discrepancy is provided in Ref. [28]. Again, it can be observed that the portions of the temperature profiles corresponding to the late particle burnout sections are rather noisy, see Fig. 8, because of the weak intensity signals, see Fig. 7.

3.4. Additional comments on the measured temperatures

Vapor phase FeO has been observed in hybrid methane-iron-air systems [10], indicative of partial evaporation of iron and subsequent vapor-phase reaction. FeO likely oxidizes and condenses to form nanoparticles of Fe_2O_3 or Fe_3O_4 [10,27]. Considering the observation that the aerosols are formed in the near-particle region, it is difficult to determine whether the micrometric particle or the nanometric aerosol particles are emitting most of the radiation. Temperatures of either of these particles can exceed the gas temperature under typical combustion conditions, but fine particles would experience faster heat loss to the envelope gas, as attested by the rather dark contrails. The temperature of the gas- nanoparticle dispersion is quickly equilibrated; both phases exist at the same temperature, but this temperature may change as mass and heat are exchanged between the gas and the nanoparticles. Radiative heat flux would very likely be reduced in a significant manner, and aerosols will distribute thermal radiation differently due to their strong scattering affinity. Aerosols would also have consequences for pyrometric temperature determination, as thermal radiation from the primary larger micrometric particle and the nanometric particles would be superimposed and a strategy to divide both parts would be needed. Furthermore, liquid iron or FeO which vaporize and react in the particle boundary layer can influence the global energy balance and the oxygen transfer to the particle surface. Regarding the energy balance it seems obvious that vapor phase reactions are fast and should allow complete formation of Fe_2O_3 in short time scales, releasing the maximum available energy as long as oxygen is sufficiently available, and the furnace gas temperature is below the decomposition temperature of Fe_2O_3 (~ 1700 K). On the other hand, this would shield the remaining parent particle from further oxidation and reduce its temperature. This in turn would reduce the evaporation rate, but heat flux from the vapor flame would still affect the particle. This effect has been investigated for coal particles [45], where the volatile flame shields the particle from oxygen, but produces heat in the particle boundary layer which influences the particle to a certain extent. More on the physics and chemistry of the combustion of the iron particles is given in [28].

3.5. Combustion durations

Combustion duration times of the single iron particles are listed in Table 1. Times are determined from the pyrometric-intensity signals and their standard deviations are derived from over 10–15 individual particle intensity profiles. Burn-times are listed both for the smaller particle size cut and for the larger size cut; they are also listed for the durations of the first detected radiation peak and for the second radiation peak, as well as the summation of the two peaks. In the range of oxygen mole fractions between 21% and 50%, shorter combustion duration times can be attributed to the higher peak combustion temperatures in the latter case. However, in the range of oxygen mole fractions between 50 and 100%, the slightly shorter combustion duration times in the latter case cannot be explained based on peak temperature, since peak temperatures are similar in both of these cases. In fact, the time durations for these particles to reach peak temperature in both of these oxygen mole fractions are comparable. The difference seems to be contributed from the tail end of their burnout (end section), which terminates faster in the neat oxygen case. Finally, in the same ambient gas, the combustion times of the larger particles are longer than those of the smaller particles, even if their peak temperatures are similar; again; with contributions to this behavior stemming from the prolonged tail end of their burnout. The longer combustion durations of the particles of the larger size cut (45–53 μm) can be correlated with the fact that their mass is nearly twice the mass of those of the smaller size cut (38–45 μm).

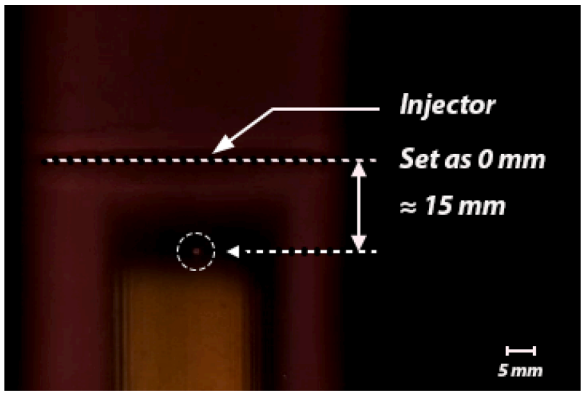

Fig. 10. Ignition delay of an 38–45 μm iron particle was deduced from the distance of the tip of the injector to the location in the furnace where the first appearance of light from the burning particle was detected.

An interesting observation is that the radiation intensity profiles of different individual iron particles burning in air are in close agreement in magnitude, whereas those burning at higher oxygen more fractions are not, see Fig. 7. In fact, such particle-to-particle intensity variability increases with increasing oxygen mole fraction. To the contrary, the corresponding temperature profiles of different individual iron particles are in good agreement in all cases. A potential explanation for this phenomenon is the occurrence of random particle combustion phenomena at increasing oxygen concentrations, such as what appears to be bursting micro-jets of molten matter from particles, which increase the projected luminous area of such particles but not their temperature. An iron particle undergoing such behavior in neat oxygen is illustrated in Fig. 9.

3.6. Particle ignition delays

The ignition delay of iron particles in the furnace was deduced from optical observations on recorded photographic profiles, as shown in Fig. 10. The distance of the igniting particle from the furnace injector was recorded and the time to ignition was calculated from the frame rate. The particle velocity was determined to be 186 mm/s. The measured “ignition delays” are defined herein as the time between the initial entrance of a (backlit) particle from the injector’s tip into the

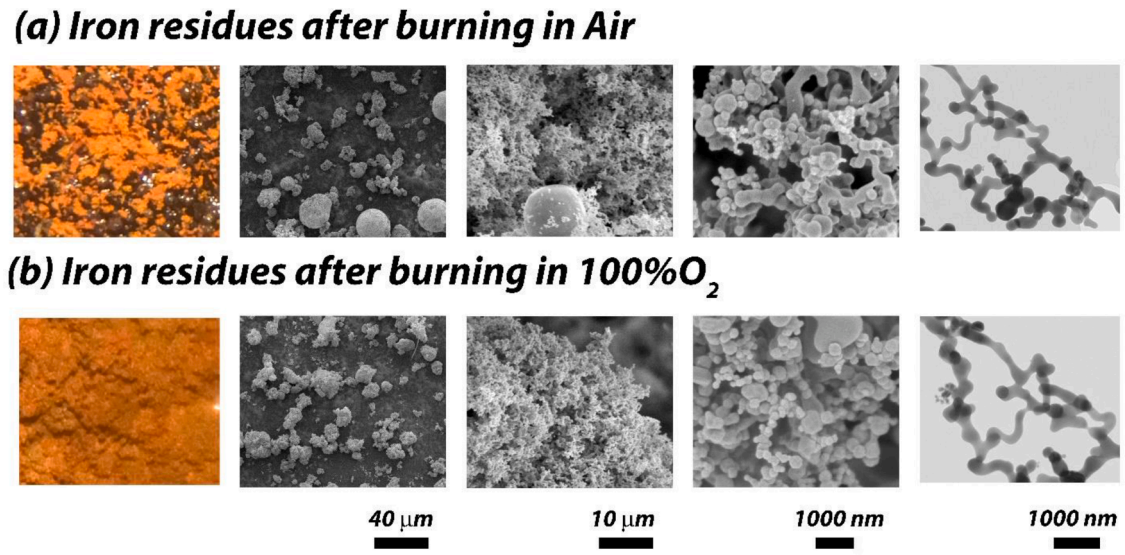

Fig. 11. From Left: Optical microscope, SEM and TEM photographs of residues from combustion of iron particles in (a) air and (b) neat oxygen, at the bottom of DTF. The collected reddish/yellow particles appear to be in the order of 50 nm.

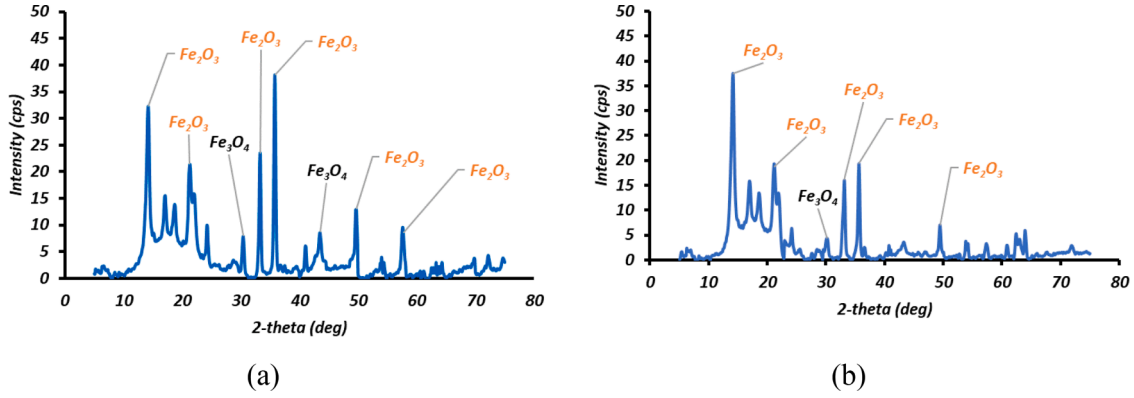

Fig. 12. X-ray diffraction spectrum of collected iron combustion product burning in (a) air and (b) 100%O_2.

furnace and the first appearance of luminous combustion (ignition by the onset of a luminous flame) [46]. Ignition delay times for ten iron particles (in the range of 38–45 μm) were measured to average 118 ± 37 ms. Moreover, ignition delay times were also obtained based on the calculated average terminal velocity (124 mm/s) to be 177±55 ms, which is a bit longer than the measured value. This is likely due to a number of assumptions that were made in this case, such as that the particle free fall took place in the Stokes regime, with a particle Reynolds number smaller than 0.1.

3.7. Ash analysis

Samples of solid-phase emissions from the combustion of streams of iron particles in air, that formed a cake on a filter at the exit of the furnace, were examined with optical microscopy, scanning electron microscopy and transmission electron microscopy, see Fig. 11. The collected particles in the cake consisted of super-micron black particles, of sizes comparable to the iron particles feedstock, and a larger number of sub-micron particles of a reddish/orange color. X-ray diffraction ($10^\circ<2\theta<80^\circ$) of these residues revealed a dominant presence of both hematite (Fe_2O_3), and magnetite (Fe_3O_4) in the case of combustion in air, see Fig. 12. Such observations are supported by the colors of the residues, which suggest that the super-micron black spheres are magnetite, whereas the red sub-micron particles are hematite.

Although the measured particle temperatures (2500–2800 K) are well-below the boiling point of the iron (3135 K), it is possible for metals to partially vaporize at lower temperatures. It has been reported that, as the partial pressure of oxygen in the gas stream increases, the thickness of the boundary diffusion layer for metal vapor decreases, resulting in an increased rate of vaporization [47,48]. The vapor species in equilibrium with a system of iron-oxygen have been reported to be only iron (Fe) and wüstite (FeO) [49]. Condensation of such species away from the iron particle surface may form a fine aerosol of in the surroundings of the burning iron spheres, as photographic evidence suggests. Further oxidation of this fine aerosol forms the collected Fe_2O_3 (hematite) particles.

4. Conclusions

The combustion behavior of single micro-metric iron particles in the size ranges of 38–45 μm and 45–53 μm was investigated in three different oxygen partial pressures (21%−100%) in nitrogen, in a constant gas temperature (1350 K) entrained furnace environment. Particle temperature profiles were measured by means of three-wavelength optical pyrometry. High-speed cinematography was used to visualize the combustion process. Samples of the combustion residue of iron were exposed to SEM, TEM and XRD to assess their structure and composition.

Experimental results revealed that the particle ignited, reached maximum luminosity while generating micro-flames of nanometric particles. Characterization of micrometric residuals showed that they

consisted of black particles of magnetite whereas nanometric residuals consisted mostly of orange-reddish powders of hematite. Increasing the oxygen mole fraction from 21% to 50% was found to increase the peak particle temperature and decrease its burnout time; however, increasing the oxygen mole fraction further from 50% to 100% had smaller effects on these parameters. Particle size increase in the aforementioned ranges did not significantly affect the peak particle temperature, under the high gas temperature condition of these experiments; but had a significant effect on particle burnout duration.

Declaration of Competing Interest

We declare that this manuscript is original, has not been published before, and is not currently being considered for publication elsewhere. We know of no conflicts of interest associated with this publication. As Corresponding Author, I confirm that the manuscript has been read and approved for submission by all the named authors.

Data availability

Data will be made available on request.

Acknowledgment

This work was partially supported by Northeastern University, the Ruhr University Research School PLUS, the Natural Sciences and Engineering Research Council of Canada, McGill Sustainability Systems Initiative (MSSI) and Canadian Space Agency through the Flights and Fieldwork for the Advancement of Science and Technology (FAST) Grant Program. The authors acknowledge Dr. Philippe Julien for input in early technical discussions and Mr. Yuan Yao for help with the pyrometric measurements.

References

[1] Braconnier A, Gallier S, Halter F, Chauveau C. Aluminum combustion in CO_2-CO-N_2 mixtures. Proc Combust Inst 2021;38:4355–63.
[2] Zhou SH, Guo P, Stolle DF. Interaction model for “shelled particles” and small-strain modulus of granular materials. J Appl Mech 2018;85:101001.
[3] Bergthorson J, Goroshin S, Soo M, Julien P, Palecka J, Frost D, Jarvis D. Direct combustion of recyclable metal fuels for zero-carbon heat and power. Appl Energy 2015;160:368–82.
[4] Bergthorson JM. Recyclable metal fuels for clean and compact zero-carbon power. Prog Energy Combust Sci 2018;68:169–96.
[5] Li S, Huang J, Weng W, Qian Y, Lu X, Aldén M, Li Z. Ignition and combustion behavior of single micron-sized iron particle in hot gas flow. Combust Flame 2022;241:112099.
[6] Shafirovich E, Mukasyan A, Thiers L, Varma A, Legrand B, Chauveau C, Gökalp I. Ignition and combustion of Al particles clad by Ni. Combust Sci Technol 2002;174:125–40.
[7] Goroshin S, Lee J, Shoshin Y. Effect of the discrete nature of heat sources on flame propagation in particulate suspensions. In: Proceedings of the Symposium (International) on Combustion. Elsevier; 1998. p. 743–9.
[8] Julien P, Vickery J, Goroshin S, Frost DL, Bergthorson JM. Freely-propagating flames in aluminum dust clouds. Combust Flame 2015;162:4241–53.
[9] Goroshin S, Palečka J, Bergthorson JM. Some fundamental aspects of laminar flames in nonvolatile solid fuel suspensions. Prog Energy Combust Sci 2022;91:100994.
[10] Julien P, Whiteley S, Goroshin S, Soo MJ, Frost DL, Bergthorson JM. Flame structure and particle-combustion regimes in premixed methane–iron–air suspensions. Proc Combust Inst 2015;35:2431–8.
[11] McRae M, Julien P, Salvo S, Goroshin S, Frost DL, Bergthorson JM. Stabilized, flat iron flames on a hot counterflow burner. Proc Combust Inst 2019;37:3185–91.
[12] Tang FD, Goroshin S, Higgins A, Lee J. Flame propagation and quenching in iron dust clouds. Proc Combust Inst 2009;32:1905–12.
[13] Tang FD, Goroshin S, Higgins AJ. Modes of particle combustion in iron dust flames. Proc Combust Inst 2011;33:1975–82.
[14] Palečka J, Sniatowsky J, Goroshin S, Higgins AJ, Bergthorson JM. A new kind of flame: observation of the discrete flame propagation regime in iron particle suspensions in microgravity. Combust Flame 2019;209:180–6.
[15] Wright A, Higgins A, Goroshin S. The discrete regime of flame propagation in metal particulate clouds. Combust Sci Technol 2016;188:2178–99.
[16] Palečka J, Goroshin S, Higgins AJ, Shoshin Y, de Goey P, Angilella J-R, Oltmann H, Stein A, Schmitz B, Verga A. Percolating reaction–diffusion waves (PERWAVES)—sounding rocket combustion experiments. Acta Astronaut 2020;177:639–51.
[17] Goroshin S, Tang FD, Higgins AJ. Reaction-diffusion fronts in media with spatially discrete sources. Phys Rev E 2011;84:027301.
[18] Wright A, Goroshin S, Higgins A. Combustion time and ignition temperature of iron particles in different oxidizing environments. In: Proceedings of the 25th international colloquium on the dynamics of explosions and reactive systems; 2015.
[19] Soo M, Mi X, Goroshin S, Higgins AJ, Bergthorson JM. Combustion of particles, agglomerates, and suspensions–a basic thermophysical analysis. Combust Flame 2018;192:384–400.
[20] Ning D, Shoshin Y, van Oijen JA, Finotello G, de Goey L. Burn time and combustion regime of laser-ignited single iron particle. Combust Flame 2021;230:111424.
[21] Ning D, Shoshin Y, van Stiphout M, van Oijen J, Finotello G, de Goey P. Temperature and phase transitions of laser-ignited single iron particle. Combust Flame 2022;236:111801.
[22] Li S, Sanned D, Huang J, Berrocal E, Cai W, Aldén M, Richter M, Li Z. Stereoscopic high-speed imaging of iron microexplosions and nanoparticle-release. Opt. Express 2021;29:34465–76.
[23] Ning D, Shoshin Y, van Oijen JA, Finotello G, de Goey LP. Critical temperature for nanoparticle cloud formation during combustion of single micron-sized iron particle. Combust Flame 2022;244:112296.
[24] Li T, Heck F, Reinauer F, Böhm B, Dreizler A. Visualizing particle melting and nanoparticle formation during single iron particle oxidation with multi-parameter optical diagnostics. Combust Flame 2022;245:112357.
[25] Tóth P, Ögren Y, Sepman A, Gren P, Wiinikka H. Combustion behavior of pulverized sponge iron as a recyclable electrofuel. Powder Technol 2020;373:210–9.
[26] Poletaev N, Khlebnikova M. Combustion of iron particles suspension in laminar premixed and diffusion flames. Combust Sci Technol 2022;194:1356–77.
[27] Rahinov I, Sellmann J, Lalanne MR, Nanjaiah M, Dreier T, Cheskis S, Wlokas Iu. Insights into the mechanism of combustion synthesis of iron oxide nanoparticles gained by laser diagnostics, mass spectrometry, and numerical simulations: a mini-review. Energy Fuels 2020;35:137–60.
[28] Fujinawa A, Jean-Philyppe J, Panahi A, Chang D, Schiemann M, Levendis YA, Bergthorson JM, Mi X. Combustion behavior of single iron particles—Part II: a theoretical analysis based on a zero-dimensional model. Under Rev Appl Energy Combust Sci 2022.
[29] Panahi A, Levendis Y, Vorobiev N, Schiemann M. Direct observations on the combustion characteristics of Miscanthus and Beechwood biomass including fusion and spherodization. Fuel Process Technol 2017;166:41–9.
[30] Khatami R, Stivers C, Joshi K, Levendis YA, Sarofim AF. Combustion behavior of single particles from three different coal ranks and from sugar cane bagasse in O_2/N_2 and O_2/CO_2 atmospheres. Combust Flame 2012;159:1253–71.
[31] Khatami R, Stivers C, Levendis YA. Ignition characteristics of single coal particles from three different ranks in O_2/N_2 and O_2/CO_2 atmospheres. Combust Flame 2012;159:3554–68.
[32] Panahi A, Tarakcioglu M, Schiemann M, Delichatsios M, Levendis YA. On the particle sizing of torrefied biomass for co-firing with pulverized coal. Combust Flame 2018;194:72–84.
[33] Panahi A, Toole N, Wang X, Levendis YA. On the minimum oxygen requirements for oxy-combustion of single particles of torrefied biomass. Combust Flame 2020;213:426–40.
[34] Panahi A, Sirumalla SK, West RH, Levendis YA. Temperature and oxygen partial pressure dependencies of the coal-bound nitrogen to NO_x conversion in O_2/CO_2 environments. Combust Flame 2019;206:98–111.
[35] Panahi A, Vorobiev N, Schiemann M, Tarakcioglu M, Delichatsios M, Levendis YA. Combustion details of raw and torrefied biomass fuel particles with individually-observed size, shape and mass. Combust Flame 2019;207:327–41.
[36] Kazanc F, Khatami R, Manoel Crnkovic P, Levendis YA. Emissions of NO_x and SO_2 from coals of various ranks, bagasse, and coal-bagasse blends burning in O_2/N_2 and O_2/CO_2 environments. Energy Fuels 2011;25:2850–61.
[37] Levendis YA, Estrada KR, Hottel HC. Development of multicolor pyrometers to monitor the transient response of burning carbonaceous particles. Rev Sci Instrum 1992;63:3608–22.
[38] Khatami R, Levendis YA. On the deduction of single coal particle combustion temperature from three-color optical pyrometry. Combust Flame 2011;158:1822–36.
[39] Condell WJ, Byrne FT. Spectral intensity of ac operated tungsten lamps. JOSA 1957;47:1135. 1131-1136.
[40] Huang J, Li S, Sanned D, Xu L, Xu S, Wang Q, et al. A detailed study on the micro-explosion of burning iron particles in hot oxidizing environments. Combust Flame 2021;238:111755.
[41] Muller M, El-Rabii H, Fabbro R. Liquid phase combustion of iron in an oxygen atmosphere. J Mater Sci 2015;50:3337–50.
[42] Glassman I. Metal combustion processes. Princeton Univ NJ James Forrestal Research Center; 1959.
[43] Krishnan S, Yugawa KJ, Nordine PC. Optical properties of liquid nickel and iron. Phys Rev B 1997;55:8201.
[44] Millot F, Rifflet JC, Wille G, Sarou-Kanian V. Density and surface tension of liquid iron oxides. High Temp High Press 2009;38:245–57.
[45] M. Thomas, H. Fletcher, S. Niksa, Heat and mass transfer in the vicinity of a devolatilizing coal particle, (1986).
[46] Mi X, Fujinawa A, Bergthorson JM. A quantitative analysis of the ignition characteristics of fine iron particles. Combust Flame 2022;240:112011.

[47] Seetharaman S. Treatise on process metallurgy, volume 3: industrial processes. Hardcover: Elsevier; 2013. ISBN: 9780080969886.
[48] Turkdogan E, Grieveson P, Darken L. Enhancement of diffusion-limited rates of vaporization of metals. J Phys Chem 1963;67:1647–54.
[49] C. Washburn, Vaporization of iron oxides (Thesis), California. Univ., Berkeley. Lawrence Radiation Lab., 1963.